# Structural and dynamical equilibrium properties of hard board-like particles in parallel confinement

Luca Tonti,[1] Fabián A. García Daza,[2] José Manuel Romero-Enrique,[3,4] and Alessandro Patti[1,4,5,a)]

[1)] *Department of Chemical Engineering, The University of Manchester, Manchester, M13 9PL, UK*

[2)] *Department of Physical, Chemical and Natural Systems, Pablo de Olavide University, 41013 Sevilla, Spain*

[3)] *Departamento de Física Atómica, Molecular y Nuclear, Área de Física Teórica, Universidad de Sevilla, Avenida de Reina Mercedes s/n, 41012 Sevilla, Spain*

[4)] *Carlos I Institute of Theoretical and Computational Physics, Fuente Nueva s/n, 18071 Granada, Spain*

[5)] *Department of Applied Physics, University of Granada, Fuente Nueva s/n, 18071 Granada, Spain*

(Dated: 22 February 2024)

We performed Monte Carlo and dynamic Monte Carlo simulations to model the diffusion of monodispersed suspensions composed of impenetrable cuboidal particles, specifically hard board-like particles (HBPs), in the presence of parallel hard walls. The impact of the walls was investigated by adjusting the size of the simulation box while maintaining constant packing fractions, fixed at $\eta = 0.150$, for systems consisting of HBPs with prolate, dual-shaped, and oblate geometries. We observed that increasing the distance between the walls led to the recovery of an isotropic bulk phase, while local particle organisation near the walls remained stable. Due to their shape, oblate HBPs exhibited a more efficient anchoring at the wall surfaces compared to prolate shapes. The formation of nematic-like particle assemblies near the walls, confirmed by theoretical calculations based on density functional theory, significantly influenced local particle dynamics. This effect was particularly pronounced to the extent that a modest portion of cuboids near the walls tended to diffuse exclusively in planes parallel to the confinement, even more efficiently than observed in the bulk regions.

## I. INTRODUCTION

Nanofluids are essentially suspensions of particles at the nanometer length scale in a liquid medium[1,2]. They have been the subject of investigation due to their ability to efficiently transfer heat compared to molecular fluids. The unique thermal and viscous properties of nanofluids make them promising candidates for a wide range of applications, including cooling systems for industrial and electronic applications[3,4], drug delivery[5,6], and the development of novel optical devices[7,8]. It has been observed that the properties of nanofluids are not only determined by the chemical nature of the components of the suspension, size, and volume fraction of the suspended nanoparticles, but also by the shape of the nanoparticles themselves[9].

Nanofluidics revolves around the study of the transport properties of nanoconfined fluids, specifically nanoparticle suspensions constrained in spaces with characteristic lengths on the order of nanometers[10]. Confined nanofluids have garnered attention for their potential applications in energy conversion systems[11], the manufacturing of filtration devices for wastewater recovery[12], and biological analysis[13]. The behaviour of confined suspensions at equilibrium has been extensively explored through theoretical studies[14–16], simulations[17–19], and experiments[20–22]. It is known that nanoparticle geometry and concentration play crucial roles in determining the self-organisation of suspensions into liquid crystalline phases of different nature[23–25]. When a suspension is confined between parallel walls, steric interactions between walls and particles, especially for certain particle shapes, can promote the capillary formation of nematic-like domains. Surface-enhanced nematisation has been observed in suspensions of cut-spheres[26], rods[27–29], and cuboids[15].

Cuboidal particles are particularly significant due to their biaxiality. By adjusting their shape from prolate to oblate geometries, a diverse spectrum of liquid crystalline phases has been observed[30,31]. Their biaxial shape positions them as ideal candidates for a deeper understanding of the interplay between translational and rotational diffusion in suspensions of anisotropic particles across various scenarios —whether at equilibrium[32,33], in the presence of external fields[34,35], or in confinement[36]. Of particular note is that when cuboids exhibit a self-dual shape (i.e., when their dimensions are related such that $W = \sqrt{LT}$, with $T$, $L$, and $W$ representing particle thickness, width, and length, respectively), they have the capability to self-assemble into biaxial nematic phases under specific conditions[37]. This property makes them especially appealing for manufacturing novel devices with unique optical features[38].

In this study, we apply stochastic simulation techniques and density functional theory (DFT) to explore the influence of planar confinement on the structural

[a)] Electronic mail: apatti@ugr.es

organisation of suspensions of hard board-like particles (HBPs) at moderate concentrations, specifically below the isotropic-to-nematic phase transition, and examine its impact on their diffusion. In particular, we performed Monte Carlo (MC) and dynamic Monte Carlo (DMC) simulations to investigate equilibrium and dynamic properties in the presence of parallel hard walls. DMC methods leverage the random nature of MC sampling algorithms to replicate the Brownian motion of colloidal particles. Originally developed for simulating pure systems[39] and later extended to mixtures[40], out-of-equilibrium phenomena[41], and systems with spatial inhomogeneities[42], this approach has proven effective in studying the dynamic and rheological properties of suspensions of anisotropic particles[43–46]. Our findings reveal that adjusting the distance between walls or varying particle geometry from prolate to dual-shaped and oblate dramatically influences the structural and dynamic properties of colloidal suspensions. These suspensions, which would exhibit typical features of isotropic fluids in the bulk, manifest capillary nematisation and surface anchoring effects near the walls. Importantly, these effects not only impact the structure but also significantly influence the local diffusive behaviour of HBPs.

## II. MODEL AND SIMULATIONS

We run MC simulations to explore the structural and dynamical properties of monodispersed suspensions of hard board-like particles (HBPs) under planar confinement. Our decision to utilise a hard-core potential stemmed from the absence of suitable soft potentials capable of accurately estimating the minimum distance between pairs of cubes or cuboids. All systems were simulated in the canonical ensemble, maintaining a constant number of particles, volume of the simulation box, and temperature. The shape of a cuboidal particle is defined by its thickness, which serves as the system unit length, width, and length. For all HBPs in our simulations, we set the thickness to $T = 1$ and the reduced length to $L^* \equiv L/T = 12$. The simulated suspensions included prolate HBPs, with a reduced width $W^* \equiv W/T = 1$, dual-shaped HBPs, with $W^* = \sqrt{L^*} \simeq 3.46$, and oblate HBPs, with $W^* = 8$. A representation of these HBPs is shown in Figure 1. In all studied systems, the packing fraction was set to $\eta = 0.15$, corresponding to regions in the bulk phase diagrams where isotropic phases are typically found[30]. The simulation box with sizes $L_x, L_y, L_z$ was flanked by two parallel hard walls positioned in the $xy$ plane, as illustrated in Figure 1. The introduction of soft walls, which would not anyway be straightforward for the lack of suitable soft potentials for cuboids, would directly impact the enthalpic contribution to the system's free energy, thereby altering the equilibrium structures, particularly in close proximity to the walls. In our system, where both wall-particle and particle-particle interactions are represented by a hard potential, the structural and dynamical properties are only determined by entropic factors or, equivalently, by excluded-volume effects. The inter-wall distance, a simulation parameter, was set to $h = \alpha L + T$, with $\alpha = \{2, 3, 4\}$. By independently adjusting the inter-wall distance and particle anisotropy, we generated nine distinct systems for analysis in this study. We set $N = 1200, 1800, 2400$ for systems with $L_z = 25T, 37T, 49T$, respectively. All simulation boxes have square cross section, e.g. $L_x = L_y$, which has been set in order to obtain $\eta$ constant for all the cases. Full details on simulation settings can be found in Section S1 of the Supplementary Information.

To investigate equilibrium properties, we performed Metropolis-based MC simulations, while dynamics was modeled using DMC algorithms. The DMC simulation technique emulates the motion of Brownian particles through a stochastic approach. Specifically, an arbitrarily set MC timestep, denoted as $\delta t_{MC}$, determines the maximum elementary displacements and rotations of the particle's center of mass and orientation axis, respectively, in accordance with the Einstein relation:

$$\delta\xi_k = \sqrt{2D_{kk}\delta t_{MC}}, \tag{1}$$

where $\delta\xi_k$ is the generic degree of freedom and $D_{kk}$ the diagonal term of the shape-dependent diffusion tensor. For this work in particular, where the dynamical properties are investigated at equilibrium, Eq. 2 is used to recover the correct Brownian-motion timescale:

$$t_{BD} = \frac{\mathscr{A}}{3}\mathscr{C}_{MC}\delta t_{MC}. \tag{2}$$

The timescale in a DMC simulation depends on the number of MC cycles, $\mathscr{C}_{MC}$, simulated (where 1 cycle is equal to $N$ random roto-translations of one particle), and the average acceptance rate $\mathscr{A}$. The link between the acceptance ratio and the unique timescale stems from the assumption (among others) of constant particle sampling volume, which limits the DMC methodology to the canonical ensemble, as used in this work. The interested reader is referred to Ref. [39] for a detailed description of the DMC method. In this work, we set $\delta t_{MC} = 10^{-5}\tau$ and $10^{-2}\tau$, where $\tau \equiv \beta T^3 \mu$ is the system unit time, $\beta$ the inverse temperature and $\mu$ the solvent viscosity (not explicitly modeled). Since the resulting difference in the acceptance rates of particles close to the wall and in the middle of the box is lower than 5%, to a good approximation it can be assumed that $\mathscr{A}$ is space-independent and Eq. 2 can be safely applied to recover the Brownian timescale (the DMC framework on space-dependent acceptance rates is discussed in Ref. [42]). Additional details on the diffusion constants of HBPs and other relevant system data are provided in the Supplementary Information. Figure 1 displays a snapshot of prolate, dual-shaped, and oblate HBPs confined within parallel walls with a distance of $h = 49T$.

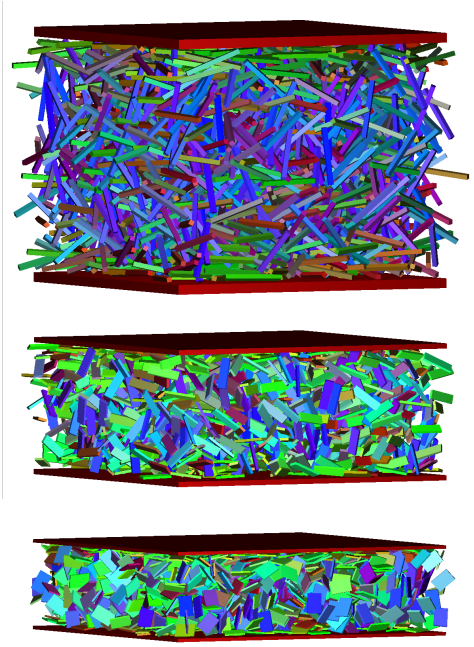

FIG. 1. Snapshots of HBPs confined in parallel walls with relative distance $h = 49T$. Systems of prolate, dual-shaped and oblate HBPs are shown in the top, centre and bottom frames of the Figure, respectively. Snapshots of dual-shaped and oblate HBPs are shown with an aspect ratio of 1:1.86 and 1:2.83 with respect to the prolate HBPs, respectively.

In order to properly characterise the structure of these systems at equilibrium, we first computed the local packing fraction in slabs parallel to the walls:

$$\eta(z) = \frac{N(z)V_p}{V}, \tag{3}$$

where $N(z)$ is the number of particles found inside a slab parallel to the walls, at distance $z$ from the bottom wall, $V_p = T \times W \times L$ is the volume of one HBP, and $V$ the volume of the simulation box. We also investigated the orientation of the particles by computing the uniaxial and biaxial order parameters, averaged over particles found in each slab. The uniaxial order parameter is defined as:

$$U_k^s(z) = \frac{1}{N(z)} \sum_{i=1}^{N(z)} P_2\left(\hat{n}_k(z) \cdot \hat{e}_{k,i}\right), \tag{4}$$

where $\hat{e}_{k,i}$ is a unit vector aligned along $k = T$, $W$ or $L$, and $\hat{n}_k(z)$, also referred to as nematic director, indicates the preferential orientation of one of the particle axes for the particles in a slab. The nematic directors and their correspondent uniaxial order parameters are obtained by diagonalisation of the following tensor:

$$\mathbb{Q}^{kk}(z) = \frac{1}{2N(z)} \sum_{i=1}^{N(z)} \left(3\left(\hat{e}_{k,i} \otimes \hat{e}_{k,i}\right) - \mathbb{I}\right). \tag{5}$$

where $\hat{e}_{k,i} \otimes \hat{e}_{k,i}$ is the outer product between the two vectors, i.e. $(\hat{e}_{k,i} \otimes \hat{e}_{k,i})_{l,m} = (\hat{e}_{k,i})_l (\hat{e}_{k,i})_m$, for $l$ and $m$ the row and column indices of the $\mathbb{Q}^{kk}$ matrix. The largest eigenvalue of $\mathbb{Q}^{kk}$ is $U_k^s$, with $\hat{n}_k$ the corresponding eigenvector, and $\mathbb{I}$ is the identity matrix. From these tensors and the nematic directors of each particle axis, we can estimate the degree of biaxiality of the system, by means of the biaxial order parameter $B_{2,k}$. Here is reported the definition of $B_{2,T}(z)$:

$$\begin{aligned} B_{2,T}(z) = \frac{1}{3}\big[&\hat{n}_W(z)\mathbb{Q}^{WW}(z)\hat{n}_W(z) + \\ &+\hat{n}_L(z)\mathbb{Q}^{LL}(z)\hat{n}_L(z) - \hat{n}_L(z)\mathbb{Q}^{WW}(z)\hat{n}_L(z) + \\ &-\hat{n}_W(z)\mathbb{Q}^{LL}(z)\hat{n}_W(z)\big]. \end{aligned} \tag{6}$$

All the other biaxial order parameters have been computed in a similar fashion[30]. By fixing the director to $\hat{z}$, which is the direction orthogonal to the walls, we estimated also $U_k^z$:

$$U_k^z(z) = \frac{1}{N(z)} \sum_{i=1}^{N(z)} P_2\left(\hat{z} \cdot \hat{e}_{k,i}\right). \tag{7}$$

which provides information on how the particle axes are oriented with respect to the walls. In the evaluation of the orientational order parameters, it has been observed that errors due to finite-size effects are proportional to $1/\sqrt{N/n_{\text{slabs}}}$, where $n_{\text{slabs}}$ is the number of slabs used to calculate the above properties between the parallel walls[47]. To limit such systematic errors, we set the number of slabs for the calculation of $U_k^s$ and $U_k^z$ equal to $n_{\text{slabs}} = 13, 19, 25$, for systems with $h/T = 25$, 37 and 49, respectively. To collect more detailed information on the particle orientation close to the wall, we estimated the probability density distribution of particle orientations, i.e. $\rho^{\omega}(\cos(\theta_k))$, calculating the dot product between one particle axis and $\hat{z}$, i.e. $\hat{z} \cdot \hat{e}_k = \cos(\theta_k)$, using only HBPs found in slabs $l_\omega$ within $3.5T$ from the surfaces of the top and bottom walls.

The dynamical properties are also evaluated in slabs, as a function of the distance from the walls. According to the particle local density distribution from one wall to the other, all systems simulated show local density fluctuations in portions of the box from the walls up to distances $\sim 12.5T$ with respect to the walls; beyond this distance, particles can either recover a bulk-like behaviour (shall the inter-wall distance be sufficiently long) or directly enter the region of influence of the opposite wall. For this reason, we studied the dynamics of HBPs in slabs parallel to the walls, by splitting the region close to the walls in several layers, and, if applies, by selecting one single slab for the entire bulk-region. The definitions and dimensions of the slabs employed in the analysis are reported in the Supplementary Information. Within each slab, we calculated the total mean-squared displacement (MSD), and the MSD in the directions parallel and perpendicular to $\hat{z}$, as follows [42]:

$$\langle \Delta r_\lambda^2(t)\rangle^l = \frac{1}{P(t)}\left\langle \frac{1}{N(0)}\sum_{i\in S_l(0,t)}\left(r_{i,\lambda}(t)-r_{i,\lambda}(0)\right)^2\right\rangle, \tag{8}$$

where $\lambda = \{z, xy, xyz\}$ refers to the dimensionality of the MSD, $P(t)$ is the "survival probability", i.e., the probability of the particles to remain in slab $l$ from time zero to time $t$, and $S_l(0,t)$ is the corresponding set of the surviving particles inside $l$ from time zero to $t$. By applying the same system of slabs, we also computed the Non-Gaussian Parameter (NGP):

$$\alpha_{2,d}^l(t) = \frac{\langle \Delta r_\lambda^4(t)\rangle^l}{c_{2,d}\left(\langle \Delta r_\lambda^2(t)\rangle^l\right)^2} - 1, \tag{9}$$

where $c_{2,d} = (1+2/d)$, with $d$ reflecting the dimensionality of the displacements analysed. In our case, $\alpha_{2,3}$ will refer to the NGP correspondent to the 3-dimensional displacement of the HBPs, with $c_{2,3} = 5/3$, while $\alpha_{2,2}$ is the NGP of the HBPs moving in $xy$ planes, parallel to the walls, and $c_{2,2} = 2$. The definition of the constant $c_{2,d}$ assumes an isotropic diffusion of the particles. In the presence of a preferential diffusion in specific directions, $c_{2,3}$ for the 3-dimensional displacement can be corrected as follows[48]:

$$c'_{2,3} = \frac{3D_{\parallel,t}^2 + 8D_{\perp,t}^2 + 4D_{\parallel,t}D_{\perp,t}}{D_{\parallel,t}^2 + 4D_{\perp,t}^2 + 4D_{\parallel,t}D_{\perp,t}}. \tag{10}$$

As can be appreciated later in the Discussion of the results, we applied Eq. 10 to properly estimate the 3-dimensional NGP of the HBPs diffusion near the walls.

Finally, following the generalised Einstein relation, that reads $\langle \Delta r_\lambda^2\rangle = 2dD_\lambda t^{\beta_\lambda}$, for non-linear diffusion of particles over time, we can estimate the apparent exponent in slabs ($\beta_\lambda^l$) according to the following formula[49]:

$$\beta_\lambda^l(t) = \frac{\mathrm{d}\log\langle \Delta r_\lambda^2(t)\rangle^l}{\mathrm{d}\log t}, \tag{11}$$

Due to the natural symmetry of our systems, arising from having two parallel flat walls containing diffusing particles at equilibrium, to improve statistics, we merged together the results obtained from opposite slabs. The so-obtained dynamical properties refer to slabs $l_\omega$ close to the wall, slabs $l_b$ where a bulk-like region is observed, and intermediate slabs $l_i$ between $l_\omega$ and $l_b$. Since we observe that the dynamics of particles with the same shape, in slabs $l_\omega$, does not change when changing the distance between the walls, we also calculated the same dynamical properties, in slabs $l_\omega$, averaging over systems with different inter-wall distances:

$$\overline{\langle \Delta r_\lambda^2(t)\rangle^\omega} = \frac{1}{3}\sum_h \langle \Delta r_\lambda^2(t)\rangle_h^\omega \tag{12}$$

$$\overline{\alpha_{2,d}^\omega}(t) = \frac{1}{3}\sum_h \alpha_{2,d}^{\omega,h}(t) \tag{13}$$

$$\overline{\beta_\lambda^\omega}(t) = \frac{1}{3}\sum_h \beta_\lambda^{\omega,h}(t) \tag{14}$$

$$\tag{15}$$

## III. THEORY

We have applied DFT to investigate the effect of confinement on the formation of nematic-like clusters and calculate the nematic order parameters that are compared with those obtained by simulation. To this end, the free-energy functional $F$ of a fluid of cuboids can be written in DFT as follows

$$\begin{aligned}\beta F &= \beta F[n] = \beta F_{\mathrm{ideal}}[n] + \beta F_{\mathrm{exc}}[n] \equiv \\ &\equiv \int_{\mathcal{V}} d\vec{r}\int d\hat{\omega}\, n(\vec{r},\hat{\omega})[\ln(n(\vec{r},\hat{\omega})\Lambda^3) - 1] + \\ &+ \int_{\mathcal{V}} d\vec{r}\, n(\vec{r},\hat{\omega})\beta\phi(\vec{r},\hat{\omega}) + \beta F_{\mathrm{exc}}[n].\end{aligned} \tag{16}$$

where $F_{\mathrm{ideal}}$ and $F_{\mathrm{exc}}$ are, respectively, the ideal and excess contributions to $F$, $\beta$ is the inverse temperature, $\Lambda = h/\sqrt{2\pi m/\beta}$ the thermal de Broglie's length, $\mathcal{V}$ the volume of the fluid of cuboids, $\phi_1(\vec{r},\hat{\omega})$ the external potential energy, $n(\vec{r},\hat{\omega})$ the local density of particles at a position $\vec{r}$ and orientation $\hat{\omega}$, and $F_{\mathrm{exc}}$ the excess free-energy contribution associated to the interactions between cuboids, which is not known in general. Minimisation of Eq. (16) with respect to the density field $n(\vec{r},\hat{\omega})$ constrained by the condition

$$\int_{\mathcal{V}} d\vec{r}\int d\hat{\omega}\, n(\vec{r},\hat{\omega}) = N, \tag{17}$$

where $N$ is the total number of cuboids, leads to the equation

$$n(\vec{r},\hat{\omega}) = \frac{1}{\Lambda^3}e^{\beta\mu-\beta\phi(\vec{r},\hat{\omega})+C_1(\vec{r},\hat{\omega};[n])}, \tag{18}$$

with $\mu$ being the Lagrange multiplier associated to Eq. (17), which can be identified as the chemical potential, and $C_1$ the one-body direct correlation function, defined as

$$C_1(\vec{r},\hat{\omega};[n]) = \beta\frac{\delta F_{\mathrm{exc}}[n]}{\delta n(\vec{r},\hat{\omega})}. \tag{19}$$

where $\delta F_{\mathrm{exc}}[n]/\delta n(\vec{r},\hat{\omega})$ is the functional derivative of $F_{\mathrm{exc}}$ at $n$. Note that $C_1$ is also dependent on the local density profile, so Eq. (18) is actually a functional equation for $n(\vec{r},\hat{\omega})$. Usually, the density profile is split

in the overall, orientation-integrated density $\rho(\vec{r})$ and the orientational distribution function $f(\vec{r},\hat{\omega})$ as

$$n(\vec{r},\hat{\omega}) = \rho(\vec{r}) f(\vec{r},\hat{\omega}). \tag{20}$$

These new functions satisfy the relationships

$$\rho(\vec{r}) = \int d\hat{\omega}\, n(\vec{r},\hat{\omega}) \quad , \quad \int d\hat{\omega}\, f(\vec{r},\hat{\omega}) = 1. \tag{21}$$

In the bulk isotropic fluid, $\phi = 0$ and $n$ does not depend on the cuboid orientation due to the rotational symmetry of the phase. Thus, $\rho = 8\pi^2 n$ and $f = 1/(8\pi^2)$ in the bulk isotropic phase. Furthermore, the density is independent of $\vec{r}$, so $C_1$ is a constant due to Eq. (18) which will be denoted as $C_1^\infty$. Thus, the overall density takes a constant value $\rho_\infty = 8\pi^2 \exp(\beta\mu + C_1^\infty)/\Lambda^3$.

Now, we assume the fluid is confined inside a slit pore of width $H$. The external potential energy is expressed as $\phi(\vec{r},\hat{\omega}) = \phi_1(z,\hat{\omega}) + \phi_1(H-z,\hat{\omega}')$, where $z$ is the normal coordinate to the confining walls, and $\hat{\omega}'$ is the mirror image of $\hat{\omega}$ with respect to the $z = 0$ plane. If the cuboid and the wall overlap, then $\phi_1 \to +\infty$, vanishing otherwise. This potential is orientation-dependent, as the cuboid-wall contact distance depends on the relative orientation of the cuboid with respect to the wall normal. In this scenario, translational symmetry along the transversal directions dictates that $n = n(z,\hat{\omega})$, i.e., $C_1 = C_1(z,\hat{\omega};[n])$. The orientational order parameters can be expressed in terms of the orientational distribution function as:

$$U_k^z(z) = \langle P_2(\hat{z}\cdot\hat{e}_k)\rangle = \int d\hat{\omega}\, f(z,\hat{\omega}) P_2(\hat{z}\cdot\hat{e}_k), \tag{22}$$

where $P_2(x)$ is the second-order Legendre polynomial, $\hat{z}$ is the unit vector normal to the walls, and $\hat{e}_k$ are the unit vectors associated to the cuboid main axes. Note that these order parameters vanish if $f(z,\hat{\omega})$ correspond to a bulk isotropic phase.

As our simulations are performed under thermodynamic conditions (i.e. chemical potential) of the system which correspond to a bulk isotropic phase, we may assume that the density profile is, in some sense, a perturbation around the bulk expression given above. This would affect mainly the one-body direct correlation function, which it is a functional of the local density field itself. Thus, as a first approximation, we could use Eq. (18) to obtain the orientation distribution by assuming that the one-body direct correlation function corresponds to an isotropic local density field, i.e. it does not depend on the cuboid orientation. Consequently, Eq. (18), together with Eq. (21), leads to the following approximate expressions for $\rho$

$$\begin{aligned}\rho(z) &= \frac{e^{\beta\mu + C_1^\infty}}{\Lambda^3} \int d\hat{\omega}\, e^{-\beta\phi(z,\hat{\omega})} = \\ &= \frac{\rho_\infty}{8\pi^2} \int d\hat{\omega}\, e^{-\beta\phi(z,\hat{\omega})}\end{aligned} \tag{23}$$

and for the orientational distribution function

$$f(z,\hat{\omega}) = \frac{e^{-\beta\phi(z,\hat{\omega})}}{\int d\hat{\omega}\, e^{-\beta\phi(z,\hat{\omega})}}. \tag{24}$$

Several key observations merit attention at this point. Firstly, within this approximation, the overall density is proportional to the bulk value, which is intimately linked to the interactions among cuboids through $C_1^\infty$ and its evaluation would necessitate a specific theoretical framework for the excess free-energy functional (such as Onsager, Parsons-Lee, etc.). Furthermore, the overall density exhibits a monotonic increase from a negligible value at the point of contact with the walls to the bulk density at distances beyond half of the cuboid's longest sidelength. On the other hand, the orientational distribution function is uniquely shaped by the wall-cuboid interaction. Notably, the expression in Eq. (24) shares similarities with the barometric formula applicable to ideal systems under external fields, notwithstanding our consideration of the interactions between cuboids. Secondly, given that $\phi$ represents a hard potential, the orientation distribution function in Eq. (24) uniformly distributes over orientations where the cuboid avoids overlapping with the walls. Consequently, at distances from the walls exceeding half the cuboid's longest side length, the isotropic orientational distribution function is reinstated. As a result, all orientational order parameters, including $U_k^z$, vanish. This concurs with the findings from computer simulations reported in this paper.

## IV. RESULTS

In this section, we examine the structural and dynamical properties of the systems under investigation. Prior to the analysis of the diffusion of HBPs, it is essential to thoroughly characterize the influence of planar confinement on the model suspensions at equilibrium.

In Figure 2, we present profiles of local packing fractions in slabs parallel to the walls, as a function of the inter-wall distance. Due to the system's geometry, these profiles display symmetry with respect to the $\Pi = (x, y, h/2)$ plane, dividing the box into two equal regions. Consequently, $\eta(z)$ from the top wall to $\Pi$ is the mirror image of $\eta(z)$ from the bottom wall to $\Pi$, regardless of particle anisotropy. Variations in $h$ do not appear to significantly impact particle organisation, except for the emergence of a bulk-like region, particularly noticeable at $h^* \equiv h/T = 49$. For $z > 12T$ (or $z > h - 12T$), all systems tend to revert to the bulk-like isotropic phase, with a gradual decay of $\eta(z)$ to approximately 0.15. The extent of this bulk region depends on the available volume between the walls. Specifically, while systems with $h^* = 25$ lack sufficient space to display a bulk region, those with $h^* = 37$ and 49 exhibit a distinct plateau in the $\eta(z)$ profile, where the influence of walls can be disregarded. Preliminary observations indicate that HBPs

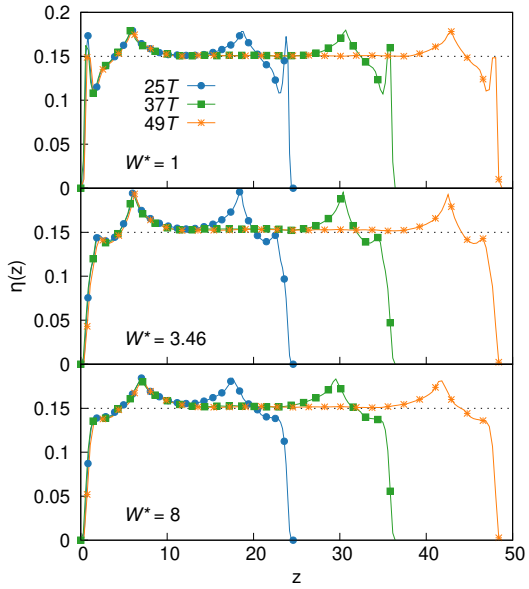


FIG. 2. Profiles of local packing fraction in slabs parallel to the walls. Top, middle and bottom frames show, respectively, the profiles obtained in systems of prolate, dual-shaped and oblate HBPs. Blue lines and circles, green lines and squares and orange lines and asterisks refer to inter-wall distances of $25T$, $37T$ and $49T$, respectively. The horizontal dotted lines at $\eta = 0.15$ highlights the total packing fraction of the systems studied.

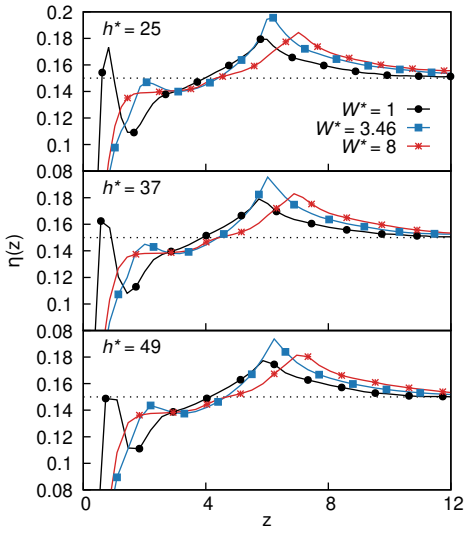


FIG. 3. Local packing fraction distributions of prolate (black lines and circles), dual-shaped (blue lines and squares) and oblate (red lines and asterisks) HBPs in the region close to the walls. Top, middle and bottom panels refer to inter-wall distances of $h^* = 25$, 37 and 49, respectively. The dotted lines at $\eta = 0.15$ highlight the total packing fraction of the system.

aggregate in the vicinity of the walls, exhibiting different patterns depending on their shape, and undergo rearrangements as the distance from the walls increases. In other words, HBPs need to span their own length $L$ to recover the orientational distribution seen in the bulk isotropic phase.

Some insights into particle orientation can be gleaned through a detailed analysis of the local packing fraction profile in the proximity of the wall. In Figure 3, we compare the local packing in the region close to the walls for the three anisotropies studied. Notably, there is no significant difference in packing fraction profiles as the separation between the walls increases, except for the first peak in the distribution of prolate cuboids. This peak slightly increases from 0.15 to 0.17 at $z/T \simeq 1$ as the walls approach each other. Prolate HBPs exhibit a higher concentration at distances less than $3T$ from the walls compared to the bulk, a phenomenon not observed for dual-shaped and oblate HBPs. This behaviour can be explained by considering how our model particles organise in the vicinity of flat hard walls. Packing of rod-like cuboids is enhanced when particles align along their main axis, a preference enforced by planar confinement and the necessity for long HBPs to be in very close proximity to the walls. The peak at $z/T \simeq 1$ in Figure 3 implies that rod-like HBPs have their main axis parallel to the wall. Although a similar behaviour would be expected for dual-shaped and oblate HBPs, they are less likely to pack closely due to their larger $WL$ faces, which occupy a surface area 3.26 and 8 times larger than that of prolate HBPs, respectively. The $\eta(z)$ profile of dual-shaped HBPs exhibits a slight peak at $z \sim 2T$, possibly indicating a partial piling of particles near the walls. However, this difference is not as pronounced as observed in systems of prolate HBPs. An increase in the $\eta(z)$ profile is observed for all particle shapes between $z/T = 6$ and 7. The particles around this local maximum are sufficiently distant from the wall to lose their wall-induced alignment, gaining more rotational freedom and gradually adopting a random orientation, as expected in an isotropic phase. It is noteworthy that the theoretical approximation given by Eq. (23) fails to capture the features observed in the packing fraction profiles. This is not unexpected, as the presence of maxima in the packing fraction profile suggests depletion effects arising from correlations between particles at various distances from the wall. In contrast, our theoretical approximation relies solely on wall-cuboid interactions to determine its dependence on $z$.

In light of these considerations, we turn our attention to the distribution of local uniaxial order parameters calculated in planar slabs. Figure 4 illustrates $U_k^z(z)$, representing the uniaxial order parameter concerning the $\hat{z}$ direction or, equivalently, perpendicular to the planar confinement (see Eq. 7). Simultaneously, Figure 5 displays the self-uniaxial order parameter $U_k^s(z)$ (see Eq. 4). Both parameters are computed with respect to particle thickness, width, and length. Specifically, $U_k^z$ provides insights into how the HBPs align with $\hat{z}$ and the walls, while $U_k^s$ reveals their alignment with each other. As discussed

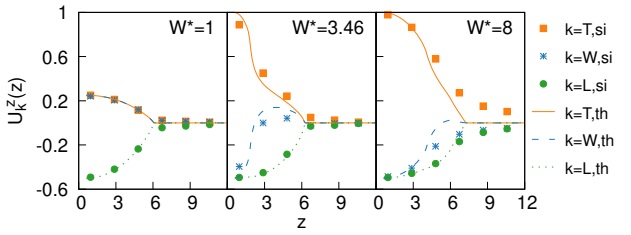


FIG. 4. Distribution of $\hat{z}$-oriented uniaxial order parameter $U_k^z$. Left, middle and right frames show, respectively, the distributions of the order parameters in fluids of prolate, dual-shaped and oblate HBPs, for systems with $h/T = 25$. Results obtained from simulations are reported as orange squares for $T$, blue asterisks for $W$ and green circles for $L$. Theoretical estimations of $U_k^z$ are shown as full orange lines for $T$, blue dashed line for $W$ and green dotted lines for $L$.

in the analysis of local packing fraction profiles, wall distances exhibit minimal, if any, influence on the structural properties of the suspensions along $z$ up to $z \sim 12T$ (or $h-12T$). Our model suspensions exhibit similar features in this range, organising themselves into the expected isotropic phase. This observation is reflected in the profiles of the self-uniaxial order parameters: the top left to top right frames (a), (d), and (c) of Figure 5 (for prolate HBPs) all show identical $U_k^s$ profiles at the extremities, reaching a consistent plateau where anticipated. Similarly, properties of dual-shaped (frames (b), (e), and (h) of Figure 5) and oblate HBPs (frames (c), (f), and (i) of Figure 5) behave likewise. For clarity, in Figure 4, we present a magnification of the total profile of $U_k^z$ in the range $0 \leq z \leq 12T$, obtained from systems with $h/T = 25$. We first analyse how HBPs orient themselves concerning the wall and then discuss their mutual organisation.

We observe that, irrespective of the system, $U_L^z$ converges to a value close to $-1/2$ near the walls and approaches approximately 0 in the bulk-like region. This reaffirms that the main particle axis is preferentially aligned perpendicularly to $\hat{z}$ in the proximity of the walls, transitioning to a random orientation as the distance from the walls increases. Different trends are noted in the orientation of the minor particle axes, aligned along $T$ and $W$, as the particle shape varies. For prolate HBPs sufficiently close to the walls, both $T$ and $W$ exhibit a subtle inclination to orient along $\hat{z}$, with $U_T^z \simeq U_W^z \simeq 0.2$ which is not significantly large. A markedly different behaviour is observed in fluids of oblate cuboids (right frame of Figure 4). Near the walls, their minor axis, aligned with $T$, is significantly oriented in the direction of $\hat{z}$ as the pronounced alignment, with $U_T^z \sim 0.8$, indicates. This behaviour is likely attributable to the large surface area of the $WL$ faces of particles, which are better packed when lying on the wall. We also note that the orientation of the two largest axes (oriented along $W$ and $L$) with respect to $\hat{z}$ follows very similar profiles. Finally, fluids of dual-shaped HBPs, akin to oblate HBPs, exhibit a strong alignment near the walls between their minor axis and $\hat{z}$, but this alignment decays to 0 at approximately $z = 5T$. Additionally, in contrast to the tendencies reported for oblate HBPs, $U_W^z$ and $U_L^z$ are markedly different close to the wall. While the former remains constantly zero at distances $z > 2T$ from the wall, revealing a random orientation of the medium axis, the latter indicates that a degree of ordering, with $L$ roughly perpendicular to $\hat{z}$, is sustained over longer distances. We believe that the ambivalent nature of dual-shaped particles, being precisely between oblate and prolate geometries, determines a behaviour that incorporates elements of both shapes, as also noted in previous works[30,32,35,46,50].

The profiles of $U_k^z$ obtained from MC simulations (points in Figure 4) are also in excellent agreement with DFT calculations (dashed lines in the same Figure). The model describes particle organisation as a perturbation of the expected isotropic behaviour in bulk. Thus, unlike the packing fraction profiles, the distribution of particle orientation recovered from DFT analysis does not depend on specific interactions between cuboids but is exclusively determined by wall-particle interactions. This assumption is sufficient to replicate the results recovered from simulations and demonstrates that capillary nematization of isotropic phases near walls naturally arises in dilute suspension, where isotropic phases are expected. Interestingly, deviations between theory and simulations, despite being small, emerge when transitioning from prolate to oblate shapes, where inter-particle interactions become more relevant for the orientation of the entire suspension.

Similar features emerge from the analysis of the self-uniaxial order parameter, $U_k^s(z)$, whose profiles are presented in Figure 5. It's important to note that $U_k^s(z)$ measures the orientation of the particle axes concerning their mean orientation, referred to as the nematic director. The definition of this vector is meaningful only if ordering is substantial. In systems of prolate HBPs, $U_T^s(z) \simeq U_W^s(z)$ over the entire inter-wall distance in the $\hat{z}$ direction (frames (a), (d), and (g)). The larger value of $U_L^s(z) \simeq 0.4$ close to the walls indicates that uniaxial nematic domains form but vanish at increasing distances. The alignment of the main axis coupled with the weaker alignment of the minor axes suggests that while nematic-like clusters can indeed form in regions close to the walls, they have a negligible degree of biaxiality and are, therefore, uniaxial. This conclusion is supported by the analysis of the biaxial order parameter $B_{2,L}(z)$ reported in the left frame of Figure 6. Dual-shaped particles exhibit significantly larger values for $U_T^s(z)$ (frames (b), (e), and (h)) close to the walls, demonstrating the existence of very well-oriented uniaxial nematics with a nematic director basically perpendicular to the walls and hence oriented along $\hat{z}$. The other two order parameters, $U_W^s(z)$ and $U_L^s(z)$, are significantly lower, indicating a dominant uniaxial character with no evidence of biaxiality (see $B_{2,T}(z)$ in the middle frame of Figure 6). Suspensions of oblate HBPs also predominantly organise

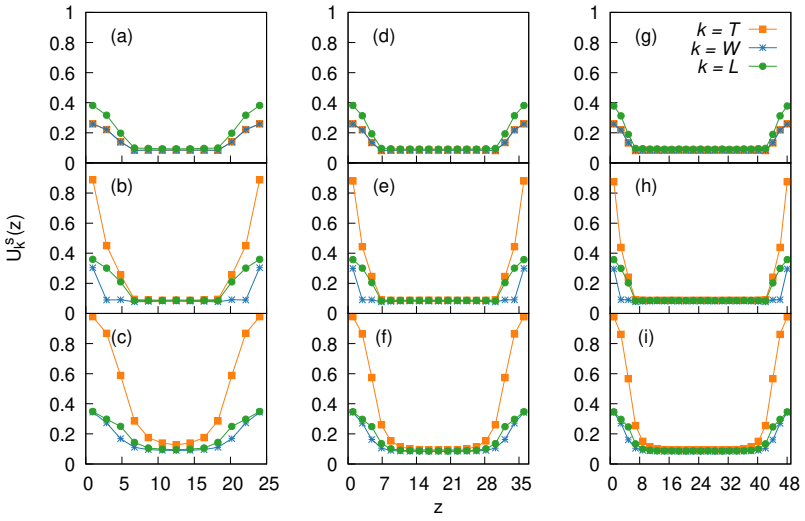


FIG. 5. Distribution of self-uniaxial order parameter $U_k^s(z)$. Each frame shows the order parameter obtained from the orientation with respect to $\hat{z}$ of the particle thickness (orange lines and squares), width (blue lines and asterisks) and length (green lines and circles), calculated in slabs parallel to the walls. Top, middle and bottom frames show, respectively, the distribution of $U_k^s(z)$ in fluids of prolate, dual-shaped and oblate HBPs. Left, middle and right frames refer to inter-wall distances equal to $h/T = 25$, 37 and 49.

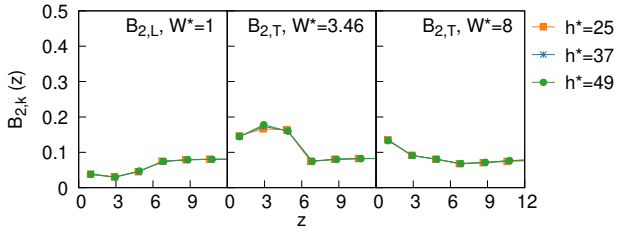


FIG. 6. Distribution of the most relevant biaxial order parameter $B_{2,k}$ for each particle shape. Left, middle and right frames show, respectively, $B_{2,L}$ of prolate, $B_{2,T}$ of dual-shaped and $B_{2,T}$ of oblate HBPs. Results obtained from systems with $h^* = 25$, 37 and 49 are reported as orange lines and squares, blue lines and asterisks, and green lines and circles.

in uniaxial nematic-like structures in the vicinity of the walls, as $B_{2,T}$ remains below 0.2 from the wall up to the middle of the box (see the right frame of Figure 6).

To gain a deeper insight into the structuring of cuboids in the region close to the walls, we calculated the probability density distribution $\rho^{\omega}(\cos(\theta_k))$ of particle orientations, where $\theta_k$ is the angle between $\hat{z}$ and $\hat{e}_k$, with $k = T$, $W$ or $L$ (see Model and Simulations Section for details). For this analysis, we considered wall-like ($l_\omega$) slabs parallel to the walls and within a distance from them of $z = 3.5T$. The results, which are practically independent of the inter-wall distance $h$, are reported in Figure 7 for prolate (top frame), dual-shaped (middle frame), and oblate (bottom frame) HBPs, and in very good (qualitative) agreement with DFT calculations. In systems of prolate HBPs, $\rho_L^{\omega}$ is peaked at $\cos\theta_L \simeq 0$, confirming the occurrence of nematic domains with $\hat{e}_L$

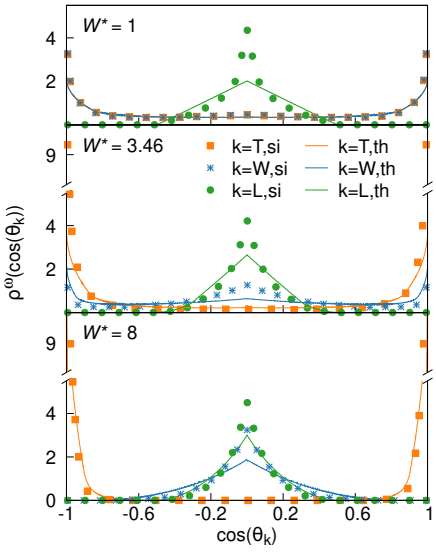


FIG. 7. Probability density distribution of particle orientations with respect to $\hat{z}$ for particles located at distance $z \leq 3.5T$ from the wall. Top, middle and bottom frames refer to systems of prolate, dual-shaped and oblate HBPs, respectively. Orange, green and blue lines and symbols refer, respectively, to $\rho_T^{\omega}$, $\rho_W^{\omega}$ and $\rho_L^{\omega}$. Solid lines and symbols refer, respectively, to DFT and simulations results. Simulations data of $\rho_T^{\omega}$ of oblate HBPs (orange squares in bottom frame) reaches $\sim 23$ at $\cos(\theta_k) = \pm 1$(out of scale).

preferentially perpendicular to $\hat{z}$, but it also exhibits a slow decay to zero, explaining the relatively low value of the nematic order parameter $U_L^s(z)$ (top frames of Figure 5). Essentially, nematic clusters form close to the

walls, but the orientation of their constituting particles is broadly distributed. The other two distributions, $\rho_T^\omega$ and $\rho_W^\omega$, behave very similarly, with peaks at $\cos\theta_T \simeq \pm 1$ and $\cos\theta_W \simeq \pm 1$, respectively, and a flat plateau elsewhere, confirming the picture of rod-like HBPs lying on the wall surface. The probability density distributions of dual-shaped and oblate HBPs share some similarities with those of prolate HBPs but also exhibit some relevant differences. While $\rho_L^\omega$ is peaked at $\cos\theta_L \simeq 0$, the other two distributions, $\rho_T^\omega$ and $\rho_W^\omega$, differ significantly from those observed in fluids of prolate HBPs. Specifically, $\rho_T^w$ exhibits a peak at $\cos\theta_T \simeq \pm 1$, especially pronounced for oblate particles, and then a flat profile throughout the remaining angular spectrum, implying a strong alignment between $\hat{e}_T$ and $\hat{z}$. In contrast, $\rho_W^\omega$ is qualitatively very similar to $\rho_L^\omega$, with a relatively less pronounced peak at $\cos\theta_T \simeq 0$. Interestingly, $\rho_W^\omega$ in fluids of dual-shaped particles is not completely flat far from the peaked region, as a minor peak is also detected at $\cos\theta_T \simeq \pm 1$, suggesting that a small number of particles might not necessarily lie on the wall surface. For all particle shapes, the DFT model replicates very well the angular distributions of $T$ and $W$, displaying remarkable agreement with simulation results. However, notable discrepancies emerge in the case of $\rho_L^\omega$, where the DFT model consistently underestimates the magnitude of the maxima. Specifically, at $\cos\theta_k = \pm 1$ for $k = T, W$ and $\cos\theta_k \sim 0$ for $k = L$, the DFT model tends to fall short. These disparities are anticipated, given that the model does not account for free energy contributions arising from inter-particle interactions.

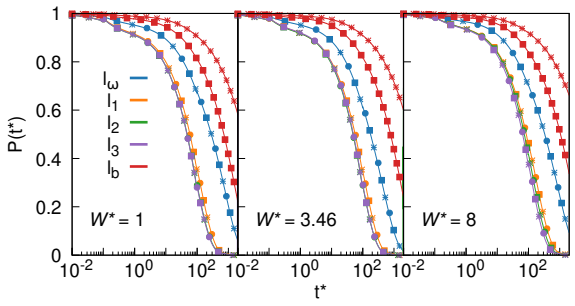


FIG. 8. Survival probabilities of prolate (left frame), dual-shaped (middle frame) and oblate (right frame) HBPs in wall-like ($l_\omega$), bulk-like ($l_b$) and intermediate ($l_i = l_{\{1,2,3\}}$) slabs parallel to the walls. The thickness of $l_\omega$ and $l_i$ slabs is, respectively, $3.5T$ and $3T$, whereas the thickness of $l_b$ slabs is $12T$ and $24T$ for inter-wall distances of $h = 37T$ and $h = 49T$, respectively. No bulk region is found in systems with $h = 25T$. Circles, squares and asterisks refer, respectively, to inter-wall distances of $h = 25T$, $37T$ and $49T$.

Not only does the presence of parallel confinement influence the local structure of our model suspensions, but it also affects their dynamical properties. To assess the extent of this effect, we divide the inter-wall spacing into parallel wall-like ($l_\omega$), bulk-like ($l_b$), and intermediate ($l_i = l_{\{1,2,3\}}$) slabs. We calculate the survival probability, $P(t)$, representing the likelihood that a given particle is found in one of these slabs over a specific time window. Specifically, $l_\omega$ and $l_i$ slabs are, respectively, $3.5T$ and $3T$ thick, while the thickness of $l_b$ slabs depends on the inter-wall distance, being $12T$ for $h = 37T$ and $24T$ for $h = 49T$. The survival probabilities are reported in Figure 8 for prolate (left frame), dual-shaped (middle frame), and oblate (right frame) HBPs as a function of $t^* \equiv t/\tau$. As a general tendency, $P(t)$ is very large up to approximately $t = 10\tau$ and then decays rapidly to zero. However, this behaviour depends on the slab geometry and vicinity to the walls. The decay of $P(t)$ in $l_i$ slabs is significantly faster than in $l_b$ slabs, simply because the latter are thicker and can retain particles for a longer time. The decay of the survival probability in $l_i$ slabs is also relatively fast when compared to that in $l_\omega$ slabs. In this case, particles can leave $l_i$ slabs from both their sides, while those in $l_\omega$ slabs have a unique way out as they are trapped at the wall face. We also notice that the dependence of $P(t)$ on the inter-wall distance $h$ is not significant for any of the three particle anisotropies. The only exception is observed in bulk-like slabs: the survival probability of particles in systems with $h = 37T$ (red squares in Figure 8) decays much faster than that of particles in systems with $h = 49T$ (red asterisks in Figure 8). This is due to the fact that the bulk-like region of the latter is twice as large as that of the former (see Supplementary Information for a thorough description of the selected slabs). While our approach to splitting the inter-wall spacing into slabs of different thickness might seem inappropriate for direct comparison of resulting survival probabilities, it is crucial for calculating dynamical properties, as explained in the following. All particles eventually leave their initial slab and diffuse through the entire fluid from wall to wall. However, they are more likely to spend a longer time in the vicinity of the wall than in the intermediate regions between them. This feature naturally arises as a consequence of the suspension nematization, driven by volume-excluded interactions of the HBPs with the walls. As we will see later, particle alignment further enhances diffusion in $xy$ planes, contributing to the survival probability in slabs near the walls. To investigate the dynamics, we focused on the most interesting regions of the system — those close to the walls and those far from them. We emphasize that all dynamically calculated properties are particularly sensitive to statistical fluctuations as they depend on the survival probability $P(t)$ of particles dwelling in a given slab. Because $P(t)_{t\to\infty} = 0$ (see Figure 8), we disregarded results at $t/\tau > 2 \cdot 10^3$ as their statistical reliability is not sufficiently robust.

In general, the bulk dynamics of hard colloidal particles in a solvent exhibit diffusive behaviour at short times, where their motion is primarily determined by random collisions with the surrounding solvent molecules. At slightly longer times, particles begin to collide with each other. If the fluid is particularly dense, they slow down significantly, delaying the decay of auto-correlation

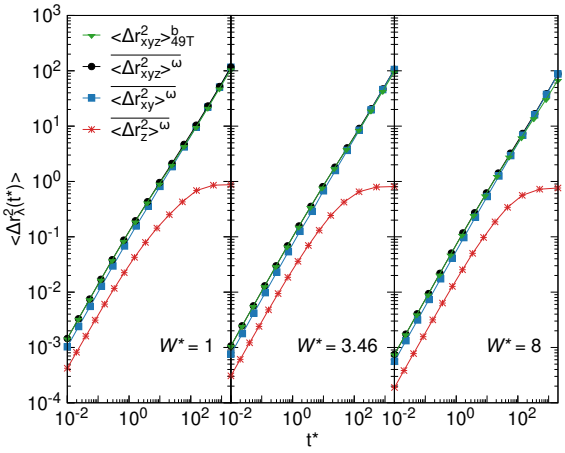


FIG. 9. MSD of HBPs in $l_b$ and $l_\omega$ slabs. Left, middle and right frames refer to the MSDs of prolate, dual-shaped and oblate cuboids, respectively. Given the weak dependence on the inter-wall distance, we averaged out each MSD in $l_\omega$ slabs obtained from systems of HBPs with $h/T = 25$, 37 and 49. Total MSD of cuboids in $l_b$ from systems with $h/T = 49$ (green triangles) has been reported for reference.

functions, and eventually return to the diffusive regime at long times. By contrast, in very dilute fluids, no crossover from short to long time scales is observed. This dynamic picture can be altered when the fluid is confined between walls, as the hindrance of undisturbed particle diffusion by the walls can redefine the boundaries of the aforementioned time regimes. To thoroughly assess the impact of planar confinement on the diffusion of our HBPs, we computed the directional mean squared displacements (MSDs) along and perpendicular to $\hat{z}$, as well as the total MSD in the three spatial directions. The results are shown in Figure 9. Given the weak dependence of the MSD on the inter-wall distance, each curve represents an average of the MSD obtained at $h/T = 25$, 37, and 49. The MSDs of prolate, dual-shaped, and oblate HBPs exhibit very similar behaviours, with no substantial dependence on particle anisotropy. Total and perpendicular MSDs calculated in $l_b$ and $l_\omega$ exhibit the typical trend of dilute colloidal suspensions, showing a single time-dependent regime where $\Delta r^2 \propto t$, spanning the five time decades of our simulations. However, the parallel MSD calculated in $l_\omega$ follows a different behaviour, bending at $t \simeq 10\tau$ and plateauing at $\Delta r_z^2(t = 10^3) \simeq 1$. This value is a very small fraction of its perpendicular counterpart, which is approximately 100 times larger. In practice, HBPs in $l_\omega$ can displace along $\hat{z}$ by either diffusing towards the wall or towards the adjacent $l_i$ slabs. This displacement, as indicated by the value of the long-time plateau, is, on average, of the order of the particle thickness and hence negligible compared to the displacement in planes perpendicular to $\hat{z}$. We therefore conclude that the particle dynamics in the regions close to the wall are mostly due to the ability of particles to diffuse laterally, in planes perpendicular to the inter-wall distance. Only when these particles enter the intermediate and bulk-like regions can isotropic diffusion be recovered.

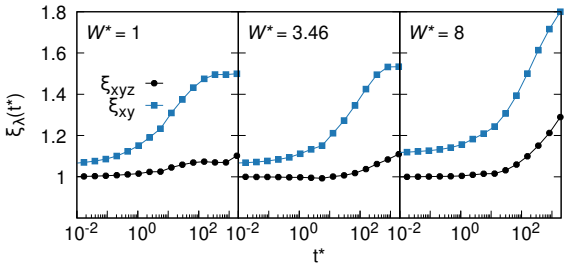


FIG. 10. Ratio between the average MSD of HBPs calculated in $l_\omega$ slabs and the MSD obtained in the bulk region of systems with $h^* = 49$. Left, middle and right frames refer, respectively, to prolate, dual-shaped and oblate HBPs. Black lines and circles refer to the total MSD, while blue lines and squares to parallel MSD. See text for additional details.

To better assess the dynamics of HBPs in $l_\omega$ slabs in comparison to that in $l_b$ slabs, we evaluate the ratios, $\xi(t)$, between the corresponding MSDs over time. Since the contribution of parallel MSDs in the regions close to the walls is negligible, these ratios are only calculated for perpendicular and total MSDs. In particular, we averaged out the dependence on $h$ of the $l_\omega$-MSDs and used the $l_b$-MSD obtained at $h^* = 49$. Mathematically, $\xi_{xy}(t) \equiv \overline{\langle \Delta r^2_{xy} \rangle^w} / \langle \Delta r^2_{xy} \rangle^b_{49T}$ and $\xi_{xyz}(t) \equiv \overline{\langle \Delta r^2_{xyz} \rangle^w} / \langle \Delta r^2_{xyz} \rangle^b_{49T}$. The results are shown in Figure 10 for prolate (left frame), dual-shaped (middle frame), and oblate (right frame) particles. Firstly, we notice that both ratios are consistently larger than 1 throughout the explored time scales, indicating that particle dynamics close to the walls is faster than that in the bulk. This is particularly evident in fluids of oblate HBPs, where $\xi_{xy} \simeq 1.8$ and $\xi_{xyz} \simeq 1.3$ at $t^* = 2 \cdot 10^3$. To understand this behaviour, one should consider the arrangement of cuboids in $l_\omega$ compared to that in the bulk. Close to the walls, cuboids are on average significantly more ordered than in the bulk, forming nematic-like clusters. This orientational order is lost in the bulk phase, which is isotropic, as the uniaxial order parameters unambiguously indicate. As found in previous works, the wall-induced isotropic-to-nematic transition triggers the formation of quasi-unidimensional channels in fluids of prolate HBPs and quasi-two-dimensional channels in fluids of oblate or dual-shaped HBPs, acting as preferential paths for their diffusion[51,52]. Additionally, we notice that $\xi_{xy} > \xi_{xyz}$ at any time, indicating that, while the dynamics in $l_\omega$ slabs is almost exclusively due to motion in planes parallel to the walls, the dynamics in the bulk is much less space-dependent, confirming the isotropic signature of the bulk phase. The results of Figure 10 are not only influenced by phase ordering but also by particle geometry, as both $\xi_{xy}$ and $\xi_{xyz}$ increase with reduced particle width, especially so at $W^* = 8$. This increase is attributed to the significant alignment that oblate HBPs achieve in $l_\omega$ slabs compared to that in the bulk, as in-

dicated by the uniaxial order parameters in Figures 4 and 5. This difference, less pronounced in fluids of prolate and dual-shaped particles, emphasizes the primary role of ordering in determining the dynamics of fluids of anisotropic particles.

In light of these considerations, we now examine the degree of deviation from Gaussianity and diffusive dynamics of cuboids by calculating the non-Gaussian parameter, $\alpha_2$, and the apparent exponent, $\beta$, defined, respectively, in Eqs. 9 and 11. The NGPs and apparent exponents calculated in $l_b$ slabs, shown in Figures 11 and 12, are in agreement with those previously obtained in systems of isotropic phases of prolate and oblate cuboids, with the same particles sizes and packing fraction used in this work, but simulated with 3D periodic boundary conditions[33]. Deviations from Gaussianity have also been investigated in liquids[53–55], glassy-forming systems[56–58], liquid crystals[59,60], and polymer melts[61]. Similar to the NGPs reported for these systems, the NGPs of Figure 11 exhibit a time-dependent behaviour across the three particle anisotropies, with a short-time tail typical of essentially Gaussian dynamics up to $t/\tau \simeq 1$, a moderate increase up to a peak located at $t/\tau \simeq 10^2$, and finally, a decay whose full relaxation is beyond our simulation time.

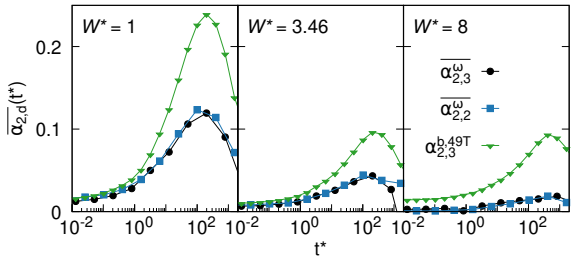


FIG. 11. Non-Gaussian parameters (NGPs) of HBPs in $l_\omega$ and $l_b$ slabs for prolate (left frame), dual-shaped (middle frame) and oblate (right frame) HBPs. Black lines and circles and blue lines and squares refer, respectively, to the 3D and 2D NGP calculated in $l_\omega$ slabs, while green lines and triangles to the 3D NGP calculated in the reference $l_b$ slab from systems with $h/T = 49$.

It is interesting to notice that the largest deviations are detected in the bulk-like region, where $\alpha^b_{2,3}$ can be up to twice as large as $\alpha^\omega_{2,3}$, highlighting the impact of ordering on dynamics and on the extent of its Gaussian signature. Due to the limited mobility along $\hat{z}$ in the regions close to the wall, we find that the 2D NGP is very similar to the 3D NGP, and, at sufficiently long times, when $D_{\parallel,t} \simeq 0$, the two are practically indistinguishable, with $\alpha^\omega_{2,2} = \alpha^\omega_{2,3}$ (see Eq. 9). The effect of particle anisotropy determines the magnitude of Gaussian deviations, with both $\alpha^b_{2,3}$ and $\alpha^\omega_{2,3}$ significantly decreasing with increasing $W^*$ from 1 (prolate HBPs) to 8 (oblate HBPs). As a general tendency, all deviations are relatively small, especially when compared to those usually observed, for instance, in colloidal glasses, crystals, and liquid crystals, where $\alpha_2$ has been found to be more than one order of magnitude larger[62–64].

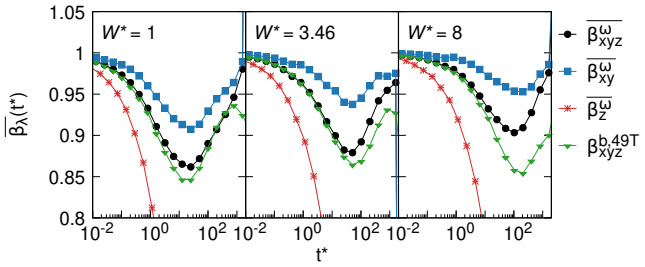


FIG. 12. Logarithmic derivative of MSDs of prolate (left frame), dual-shaped (middle frame) and oblate (right frame) HBPs in $l_\omega$ and $l_b$ slabs. Black lines and circles, blue lines and squares and red lines and asterisks refer, respectively, to the total, perpendicular and parallel apparent exponents calculated in $l_\omega$ slabs, while green lines and triangles refer to the 3D apparent exponent calculated in the reference $l_b$ slab from systems with $h/T = 49$.

While the NGP estimates the extent of Gaussian deviations in particle diffusion, the apparent exponent $\beta$, defined in Eq. 14 and shown in Figure 12, provides information on how diffusion eventually deviates from Fickianity. Fickian behaviour is characterised by an MSD that increases linearly with time, i.e., $\langle \Delta r^2 \rangle \propto t$. Diffusion of thermally agitated particles whose displacements are Gaussian-distributed and whose MSD increases linearly with time is commonly referred to as Brownian motion[65]. For all particle anisotropies, the apparent exponents calculated in the bulk, $\beta^b$, and close to the walls, $\beta^\omega$, decrease at short to intermediate times, reaching a minimum between $t = 10\tau$ and $10^2\tau$, and then increase again at long times. Over at least four time decades, the MSD is not linear with time, and it follows a power law of the type $\langle \Delta r^2 \rangle \propto t^\gamma$, with $\gamma < 1$, indicating subdiffusive behaviour that is temporary in the bulk but definitive near the walls (see also Figure 9). Due to the presence of the walls, all $\beta^\omega_z$ (red asterisks) decay to zero from short times and do not recover initial values for the entire simulated timescale. On the contrary, diffusion in $xy$ planes shows a weaker character near the walls than in the bulk region, indicating that induced particle structural organisation promotes diffusion along specific directions. Consequently, the 3D diffusion from the wall ($\beta^w_{xyz}$, black circles) to the bulk ($\beta^w_{xyz}$, green triangles) changes, and that difference in behaviour varies with changes in particle width. Over these time decades, where $\beta < 1$, we also observe that $\alpha_2 > 0$ and therefore that the dynamics is not Fickian and not Gaussian. Eventually, the system recovers its Brownian-like signature at $t/\tau > 10^3$, which is beyond our simulation time. No evidence of FNG is therefore detected.

## V. CONCLUSIONS

In summary, we have investigated the interplay between planar confinement and particle anisotropy in the self-assembly and dynamics of colloidal board-like particles. The presence of confinement induces local structural inhomogeneities and the occurrence of nematic-like domains in the regions adjacent to the walls and at volume fractions at which, in the bulk, only isotropic phases would form. While we have explored different inter-wall distances, their effect on structural and dynamical properties is not significant apart from reducing the extension of the bulk-like region in between. The influence of walls on local nematization is further supported by a straightforward DFT approach. Although the DFT approach slightly underestimates ordering at intermediate distances between walls and the bulk, it otherwise exhibits excellent quantitative agreement with the simulation results. Notably, this alignment is achieved despite the DFT model not fully capturing the features of the packing fraction profile. While being induced by confinement, structural and dynamical properties of the nematic domains are strongly influenced by shape anisotropy, with oblate particles more prone to align than their prolate counterparts. The dynamics in the region close to the walls stems from such a local organisation, with cuboids, due to their layering, diffusing preferentially in planes parallel to the walls and exhibiting a sub-diffusive behaviour in the direction perpendicular to them. As also noticed in previous studies[51,52], ordering favours the formation of preferential pathways that enhance diffusion as compared to that in the bulk, where an isotropic phase is found. The analysis of the non-Gaussian parameter $\alpha_2$ and the apparent exponent $\beta$ reveals the occurrence of sub-diffusive dynamics that intercalates between the short-time and the long-time diffusive behaviour. The latter is not however achieved in the regions close to the walls as it takes longer than the decay to zero of the particle survival probability. As a final note, we stress that our results have been obtained for hard-core model particles at equilibrium. Thanks to dynamic Monte Carlo methods we can easily simulate discontinuous interaction potentials, but, at the same time, we remind the reader of its underlying assumptions and its consequent limitations. We are currently working to incorporate the effect of fluid-mediated interactions between particles and between particles and walls. Although, to the best of our knowledge, soft cuboidal particles (and many others with a biaxial geometry) lack a suitable force field and are often modelled as arrays of spherical beads, it would be interesting to add soft inter-particle and particle-wall interactions, in order to have a more realistic description of these systems. Last, the study reported in this work could be extended to polydispersed suspensions, whose properties can be compared with previous work on similar systems[25,37,66].

## VI. SUPPLEMENTARY MATERIAL

The supplementary material includes details on the simulation parameters and the definition of the slabs used for the calculation of the dynamical properties of the suspensions in confinement.

## VII. ACKNOWLEDGEMENTS

LT, FAGD and AP acknowledge the Leverhulme Trust Research Project Grant RPG-2018-415 and the use of the Computational Shared Facility at the University of Manchester. AP acknowledges grant PID2022-136540NB-I00 funded by MCIN/AEI/10.13039/501100011033 and ERDF *A way of making Europe*; grant P21_00015 funded by Junta de Andalucía - Consejería de Universidad, Investigación e Innovación; and a María Zambrano Senior fellowship, funded by the NextGenerationEU/PRTR program. JMRE acknowledges grant PID2021-126348NB-I00 funded by Ministerio de Ciencia e Innovación.

## DATA AVAILABILITY STATEMENT

The data that support the findings of this study are available from the corresponding author upon reasonable request.

[1] J. Li, X. Zhang, B. Xu, and M. Yuan, "Nanofluid research and applications: A review," International Communications in Heat and Mass Transfer **127**, 105543 (2021).

[2] H. Mercan, "Chapter 3 - thermophysical and rheological properties of hybrid nanofluids," in *Hybrid Nanofluids for Convection Heat Transfer*, edited by H. M. Ali (Academic Press, 2020) pp. 101–142.

[3] K. V. Wong and O. D. Leon, "Applications of nanofluids: Current and future," Advances in Mechanical Engineering **2**, 519659 (2010).

[4] S. Kakaç and A. Pramuanjaroenkij, "Review of convective heat transfer enhancement with nanofluids," International Journal of Heat and Mass Transfer **52**, 3187–3196 (2009).

[5] Y. Enjavi, M. A. Sedghamiz, and M. R. Rahimpour, "Chapter 19 - application of nanofluids in drug delivery and disease treatment," in *Nanofluids and Mass Transfer*, edited by M. R. Rahimpour, M. A. Makarem, M. R. Kiani, and M. A. Sedghamiz (Elsevier, 2022) pp. 449–465.

[6] D. Mandal, K. Anand, and P. K. Prabhakar, "Biomedical applications of nanofluids in drug delivery," in *Novel Technologies in Biosystems, Biomedical & Drug Delivery*, edited by S. Kulkarni, A. K. Haghi, and S. Manwatkar (Springer Nature Singapore, Singapore, 2023) pp. 105–124.

[7] T. B. Gorji and A. Ranjbar, "A review on optical properties and application of nanofluids in direct absorption solar collectors (dascs)," Renewable and Sustainable Energy Reviews **72**, 10–32 (2017).

[8] R. A. Taylor, T. P. Otanicar, Y. Herukerrupu, F. Bremond, G. Rosengarten, E. R. Hawkes, X. Jiang, and S. Coulombe, "Feasibility of nanofluid-based optical filters," Appl. Opt. **52**, 1413–1422 (2013).

[9] I. Zahmatkesh, M. Sheremet, L. Yang, S. Z. Heris, M. Sharifpur, J. P. Meyer, M. Ghalambaz, S. Wongwises, D. Jing, and O. Mahian, "Effect of nanoparticle shape on the performance of

thermal systems utilizing nanofluids: A critical review," Journal of Molecular Liquids **321**, 114430 (2021).
[10]Y. Xu, "Nanofluidics: A new arena for materials science," Advanced Materials **30**, 1702419 (2018).
[11]Z. Zhang, L. Wen, and L. Jiang, "Nanofluidics for osmotic energy conversion," Nature Reviews Materials **6**, 622–639 (2021).
[12]M. Shahbabaei and D. Kim, "Advances in nanofluidics for water purification and filtration: molecular dynamics (md) perspective," Environ. Sci.: Nano **8**, 2120–2151 (2021).
[13]K. Yamamoto, N. Ota, and Y. Tanaka, "Nanofluidic devices and applications for biological analyses," Analytical Chemistry **93**, 332–349 (2021).
[14]I. Rodríguez-Ponce, J. M. Romero-Enrique, and L. F. Rull, "Orientational transitions in a nematic liquid crystal confined by competing surfaces," Phys. Rev. E **64**, 051704 (2001).
[15]R. Aliabadi, S. Nasirimoghadam, and H. H. Wensink, "Evidence of *t*-type structures of hard square boards in capillary confinement," Phys. Rev. E **107**, 054117 (2023).
[16]S. Nasirimoghadam, M. Moradi, and R. Aliabadi, "Biaxial planar nematic layered structures of highly confined prolate hard ellipsoids," Physica A: Statistical Mechanics and its Applications **598**, 127371 (2022).
[17]C. Anquetil-Deck, D. J. Cleaver, and P. I. C. Teixeira, "Ordering of oblate hard particles between hybrid penetrable walls," The Journal of Physical Chemistry B **124**, 7709–7716 (2020).
[18]G. J. Carlos Avendaño and H. H. Wensink, "Nanorings in planar confinement: the role of repulsive surfaces on the formation of lacuna smectics," Molecular Physics **116**, 2901–2910 (2018).
[19]A. Malijevský and S. Varga, "Phase behaviour of parallel hard rods in confinement: an onsager theory study," Journal of Physics: Condensed Matter **22**, 175002 (2010).
[20]P. Bazazi and S. H. Hejazi, "Wetting dynamics of nanoparticle dispersions: From fully spreading to non-sticking and the deposition of nanoparticle-laden surface droplets," ACS Applied Materials & Interfaces **14**, 20280–20290 (2022).
[21]V. Flauraud, M. Mastrangeli, G. D. Bernasconi, J. Butet, D. T. L. Alexander, E. Shahrabi, O. J. F. Martin, and J. Brugger, "Nanoscale topographical control of capillary assembly of nanoparticles," Nature Nanotechnology **12**, 73–80 (2017).
[22]Y. Huang, W. Li, M. Qin, H. Zhou, X. Zhang, F. Li, and Y. Song, "Printable functional chips based on nanoparticle assembly," Small **13**, 1503339 (2017).
[23]S. C. Glotzer and M. J. Solomon, "Anisotropy of building blocks and their assembly into complex structures," Nature Materials **6**, 557–562 (2007).
[24]A. Cuetos and B. Martínez–Haya, "Liquid crystal phase behavior of hard oblate spherocylinders," AIP Conference Proceedings **1091**, 234–236 (2009).
[25]M. R. Khadilkar, U. Agarwal, and F. A. Escobedo, "Phase behavior of binary mixtures of hard convex polyhedra," Soft Matter **9**, 11557–11567 (2013).
[26]M. M. Piñeiro, A. Galindo, and A. O. Parry, "Surface ordering and capillary phenomena of confined hard cut-sphere particles," Soft Matter **3**, 768–778 (2007).
[27]L. Wu, A. Malijevský, C. Avendaño, E. A. Müller, and G. Jackson, "Demixing, surface nematization, and competing adsorption in binary mixtures of hard rods and hard spheres under confinement," The Journal of Chemical Physics **148**, 164701 (2018).
[28]T. H. T. Nguyen, F. Sciortino, and C. D. Michele, "Self-assembly-driven nematization khanh," (2014).
[29]M. Dijkstra, R. v. Roij, and R. Evans, "Wetting and capillary nematization of a hard-rod fluid: A simulation study," Phys. Rev. E **63**, 051703 (2001).
[30]A. Cuetos, M. Dennison, A. Masters, and A. Patti, "Phase behaviour of hard board-like particles," Soft Matter **13**, 4720–4732 (2017).
[31]B. S. John and F. A. Escobedo, "Phase behavior of colloidal hard tetragonal parallelepipeds (cuboids): A monte carlo simulation study," The Journal of Physical Chemistry B **109**, 23008–23015 (2005).
[32]A. Cuetos and A. Patti, "Dynamics of hard colloidal cuboids in nematic liquid crystals," Phys. Rev. E **101**, 052702 (2020).
[33]L. Tonti, F. A. García Daza, and A. Patti, "Diffusion of globular macromolecules in liquid crystals of colloidal cuboids," Journal of Molecular Liquids **338**, 116640 (2021).
[34]E. Mirzad Rafael, L. Tonti, D. Corbett, A. Cuetos, and A. Patti, "Dynamics of uniaxial-to-biaxial nematics switching in suspensions of hard cuboids," Physics of Fluids **33**, 067115 (2021).
[35]Álvaro Rodríguez-Rivas, A. Patti, and A. Cuetos, "Dynamics in field-induced biaxial nematic liquid crystals of board-like particles," Journal of Molecular Liquids **367**, 120371 (2022).
[36]A. Patti and A. Cuetos, "Dynamics of colloidal cubes and cuboids in cylindrical nanopores," Physics of Fluids **33**, 097103 (2021).
[37]E. Mirzad Rafael, D. Corbett, A. Cuetos, and A. Patti, "Self-assembly of freely-rotating polydisperse cuboids: unveiling the boundaries of the biaxial nematic phase," Soft Matter **16**, 5565–5570 (2020).
[38]P. W. Benzie, D. Corbett, and S. J. Elston, "Simulation of the viewing properties and optical compensation of the biaxial nematic in-plane switching mode," Appl. Opt. **51**, 75–83 (2012).
[39]A. Patti and A. Cuetos, "Brownian dynamics and dynamic monte carlo simulations of isotropic and liquid crystal phases of anisotropic colloidal particles: A comparative study," Physical Review E **86**, 011403 (2012).
[40]A. Cuetos and A. Patti, "Equivalence of brownian dynamics and dynamic monte carlo simulations in multicomponent colloidal suspensions," Physical Review E **92**, 022302 (2015).
[41]D. Corbett, A. Cuetos, M. Dennison, and A. Patti, "Dynamic monte carlo algorithm for out-of-equilibrium processes in colloidal dispersions," Physical Chemistry Chemical Physics **20**, 15118–15127 (2018).
[42]F. A. García Daza, A. Cuetos, and A. Patti, "Dynamic monte carlo simulations of inhomogeneous colloidal suspensions," Phys. Rev. E **102**, 013302 (2020).
[43]F. A. García Daza, A. M. Puertas, A. Cuetos, and A. Patti, "Insight into the viscoelasticity of self-assembling smectic liquid crystals of colloidal rods from active microrheology simulations," Journal of Chemical Theory and Computation **0**, null (0).
[44]F. A. García Daza, A. M. Puertas, A. Cuetos, and A. Patti, "Microrheology of isotropic and liquid-crystalline phases of hard rods by dynamic monte carlo simulations," Journal of Molecular Liquids **365**, 120146 (2022).
[45]D. Cywiak, A. Gil-Villegas, and A. Patti, "Long-time relaxation dynamics in nematic and smectic liquid crystals of soft repulsive colloidal rods," Phys. Rev. E **105**, 014703 (2022).
[46]E. M. Rafael, L. Tonti, F. A. G. Daza, and A. Patti, "Active microrheology of colloidal suspensions of hard cuboids," Phys. Rev. E **106**, 034612 (2022).
[47]L. Wu, A. Malijevský, C. Avendaño, E. A. Müller, and G. Jackson, "Demixing, surface nematization, and competing adsorption in binary mixtures of hard rods and hard spheres under confinement," J. Chem. Phys. **148**, 164701 (2018).
[48]A. Cuetos, N. Morillo, and A. Patti, "Fickian yet non-gaussian diffusion is not ubiquitous in soft matter," Phys. Rev. E **98**, 042129 (2018).
[49]M. Cieśla, E. Gudowska-Nowak, F. Sagués, and I. M. Sokolov, "Tracer diffusion inside fibrinogen layers," The Journal of Chemical Physics **140**, 044706 (2014).
[50]E. Mirzad Rafael, *Phase Behaviour and Dynamics of Colloidal Liquid Crystals of Board-like Particles*, Phd thesis, The University of Manchester (2021).
[51]N. Morillo, A. Patti, and A. Cuetos, "Brownian dynamics simulations of oblate and prolate colloidal particles in nematic liquid crystals," The Journal of Chemical Physics **150**, 204905 (2019).
[52]Á. Rodríguez-Rivas, A. Patti, and A. Cuetos, "Dynamics in field-induced biaxial nematic liquid crystals of board-like particles," Journal of Molecular Liquids **367**, 120371 (2022).
[53]W. Kob, C. Donati, S. J. Plimpton, P. H. Poole, and S. C. Glotzer, "Dynamical heterogeneities in a supercooled lennard-jones liquid," Phys. Rev. Lett. **79**, 2827–2830 (1997).

[54]M. M. Hurley and P. Harrowell, "Non-Gaussian behavior and the dynamical complexity of particle motion in a dense two-dimensional liquid," The Journal of Chemical Physics **105**, 10521–10526 (1996).
[55]J. Šlepavičius, C. Avendaño, B. O. Conchúir, and A. Patti, "Structural relaxation dynamics of colloidal nanotrimers," Phys. Rev. E **106**, 014604 (2022).
[56]P. Chaudhuri, L. Berthier, and W. Kob, "Universal nature of particle displacements close to glass and jamming transitions," Phys. Rev. Lett. **99**, 060604 (2007).
[57]B. Vorselaars, A. V. Lyulin, K. Karatasos, and M. A. J. Michels, "Non-gaussian nature of glassy dynamics by cage to cage motion," Phys. Rev. E **75**, 011504 (2007).
[58]F. Rusciano, R. Pastore, and F. Greco, "Fickian non-gaussian diffusion in glass-forming liquids," Phys. Rev. Lett. **128**, 168001 (2022).
[59]M. Bier, R. van Roij, M. Dijkstra, and P. van der Schoot, "Self-diffusion of particles in complex fluids: Temporary cages and permanent barriers," Phys. Rev. Lett. **101**, 215901 (2008).
[60]E. Grelet, M. P. Lettinga, M. Bier, R. van Roij, and P. van der Schoot, "Dynamical and structural insights into the smectic phase of rod-like particles," Journal of Physics: Condensed Matter **20**, 494213 (2008).
[61]J. T. Kalathi, U. Yamamoto, K. S. Schweizer, G. S. Grest, and S. K. Kumar, "Nanoparticle diffusion in polymer nanocomposites," Phys. Rev. Lett. **112**, 108301 (2014).
[62]A. Patti, D. El Masri, R. van Roij, and M. Dijkstra, "Stringlike clusters and cooperative interlayer permeation in smectic liquid crystals formed by colloidal rods," Phys. Rev. Lett. **103**, 248304 (2009).
[63]Z. Zheng, F. Wang, and Y. Han, "Glass transitions in quasi-two-dimensional suspensions of colloidal ellipsoids," Phys. Rev. Lett. **107**, 065702 (2011).
[64]B. van der Meer, W. Qi, J. Sprakel, L. Filion, and M. Dijkstra, "Dynamical heterogeneities and defects in two-dimensional soft colloidal crystals," Soft Matter **11**, 9385–9392 (2015).
[65]A. Einstein, "Über die von der molekularkinetischen theorie der wärme geforderte bewegung von in ruhenden flüssigkeiten suspendierten teilchen," Annalen der Physik **322**, 549–560 (1905).
[66]N. Mohammad Mehdipour, N. Reddy, R. J. Shor, and G. Natale, "Orientation dynamics of anisotropic and polydisperse colloidal suspensions," Physics of Fluids **34**, 083317 (2022), https://pubs.aip.org/aip/pof/article-pdf/doi/10.1063/5.0101702/16574649/083317_1_online.pdf.